ACS Energy LETTERS

http://pubs.acs.org/journal/aelccp

Letter

# Near-Field Effects on Cathodoluminescence Outcoupling in Perovskite Thin Films

Robin Schot,* Imme Schuringa,* Álvaro Rodríguez Echarri, Lars Sonneveld, Tom Veeken, Yang Lu, Samuel D. Stranks, Albert Polman, Bruno Ehrler, and Saskia Fiedler

Cite This: *ACS Energy Lett.* 2026, 11, 3274−3281

Read Online

ACCESS | Metrics & More | Article Recommendations | Supporting Information

**ABSTRACT:** Halide perovskite semiconductors are promising materials for high-efficiency solar cells. Their optical properties can vary within and between crystallographic grains. We present spatially resolved cathodoluminescence (CL) spectroscopy at 2 and 5 keV on polycrystalline $CsPbBr_3$ perovskite films to study these variations at the nanoscale. The CL maps show a strongly reduced intensity near the polycrystalline grain boundaries. We perform numerical simulations of the far-field emission of the electron beam-generated optical near fields by using the surface profiles from AFM as input. We find that near grain boundaries the light outcoupling is strongly reduced due to enhanced internal reflection and light trapping at the curved surfaces. Lateral variations in CL intensity inside grains are due to Fabry−Pérot-like resonances in the film, with the substrate acting as a back reflector. Our results show that near-field coupling and interference effects can dominate nanoscale luminescence maps of halide perovskite films. The results are broadly relevant for the analysis of CL and the photoluminescence of corrugated thin films.

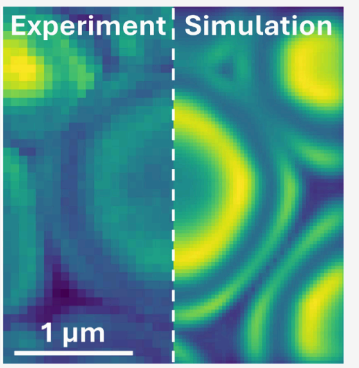


Downloaded via AMOLF on June 15, 2026 at 14:55:32 (UTC).
See https://pubs.acs.org/sharingguidelines for options on how to legitimately share published articles.

Halide perovskite semiconductors have emerged as a promising material for efficient solar cells with conversion efficiencies above 26%.[1] Perovskite solar cells are fabricated from polycrystalline thin films made from grains that are a few hundred nanometers to micrometers in size. To further increase the conversion efficiency and stability of perovskite devices, a detailed understanding of the influence of this microstructure on optoelectronic properties such as the bandgap, carrier lifetime, and recombination processes is required. In particular, measurements near grain boundaries are important, as these sites are known to act as nonradiative recombination sites, limiting optoelectronic device performance.[2,3]

Cathodoluminescence (CL) spectroscopy is a well-established technique to study the optoelectronic properties of semiconductors at high spatial resolution. In CL, a high-energy electron beam is raster-scanned over the surface, generating a cascade of inelastic scattering events inside the material. The electron beam generates a dense cloud of excited charge carriers, which then diffuse and recombine, the latter either by radiative emission (i.e., resulting in CL) or nonradiative recombination. Previous CL studies on perovskite thin films have helped identify halide segregation,[4] which results in spatial variations of the bandgap.[5] Also, variations in the CL signal have been observed between different crystal grains, indicating that the structure of the perovskite films can be laterally inhomogeneous.[3,6] Time-resolved CL has been used to probe the sub-nanosecond decay of the charge carrier population in $CsPbBr_3$ perovskite films, which was attributed to the fast diffusion of carriers away from the small electron−sample interaction volume.[7] Similarly, in other photovoltaic semiconductors, such as kesterite thin films, CL spectroscopy has proven to be a powerful technique to study inhomogeneities in materials quality.[8,9]

Spatially resolved CL maps represent the CL intensity measured at each position of the electron beam on the sample. However, on the corrugated surfaces common to halide perovskite films, the outcoupling of CL emission can be strongly influenced by the surface. In particular, transmission through the surface interface must satisfy electromagnetic boundary conditions given by Maxwell's equations that depend on the orientation of the electromagnetic fields inside the semiconductor relative to the surface. As CL is generated in a volume smaller than the wavelength of light, the CL outcoupling cannot be described by geometric ray optics but is governed by radiation from the optical near fields. Therefore, the evanescent electromagnetic near-field components must be considered in analyzing the CL maps.

In this work, we perform spatially resolved CL spectroscopy on polycrystalline $CsPbBr_3$ perovskite films. We find that the collected CL intensity is strongly reduced for electron beam positions near grain boundaries. Comparing the CL maps with

**Received:** December 15, 2025
**Revised:** February 12, 2026
**Accepted:** February 19, 2026
**Published:** March 6, 2026

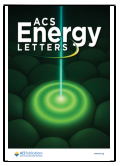


© 2026 American Chemical Society

https://doi.org/10.1021/acsenergylett.5c04161
*ACS Energy Lett.* 2026, 11, 3274−3281

atomic force microscopy (AFM) maps on the same area and using numerical simulations of the light outcoupling, we find that the reduced intensity at grain boundaries is directly related to their morphology. Reduced outcoupling of the CL emission at these points is due to internal reflection of evanescent optical near fields. We also find that measured lateral CL intensity variations across the perovskite grains are due to the interference of light reflected at the top surface of the film and substrate interface. These spatial variations, therefore, need to be taken into account when interpreting the spatially resolved CL emission from perovskite films.

To study the correlation between microstructure and the CL signal, we use a thermally co-evaporated polycrystalline $CsPbBr_3$ film on silicon with a nominal thickness of 300 nm (see Experimental Section). This composition is relatively stable under electron beam irradiation, making it ideal for isolating optoelectronic effects with minimal beam degradation.[10−12] Characteristic X-ray diffractograms (XRD) for both unannealed and annealed samples are shown in Figure S1 in the Supporting Information (SI), indicating that $CsPbBr_3$ is in the orthorhombic phase.[13−15] We used different annealing protocols to enhance the crystallinity of the films and create films with different grain sizes.

Figure 1(a−c) shows the atomic force microscopy (AFM), secondary electron (SE), and polychromatic CL maps of the same area of the $CsPbBr_3$ perovskite film. The SE image and CL map were simultaneously acquired with an acceleration voltage of 5 kV. The AFM map and SE image reveal a structure with grain sizes ranging from ∼100 nm to ∼1 $\mu$m. The AFM map shows surface height variations of up to 120 nm across the surface topography. A characteristic CL spectrum of a grain interior (single pixel) is shown in Figure 1(d), revealing an emission peak around $\lambda$ = 525 ± 3 nm (∼2.36 eV) at the bandgap of $CsPbBr_3$.[16] The dark, optically inactive grains observed in the CL map can be attributed to perovskite in the $CsPb_2Br_5$ phase, as evidenced by the XRD diffraction patterns in Figure S1.[13,14,17] Otherwise, the peak CL intensity within the grains is relatively consistent across the image, suggesting good homogeneity in the optical properties of the perovskite film across different grains.

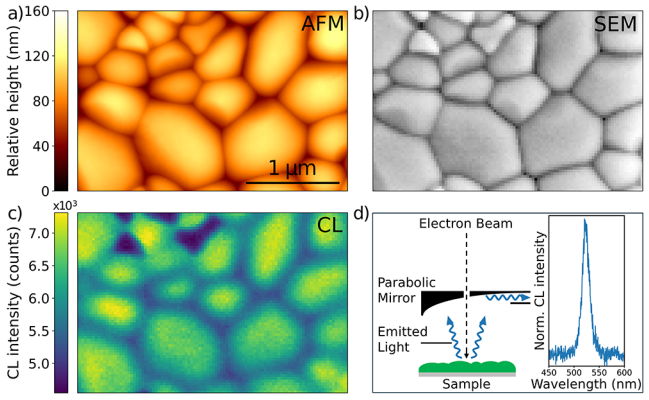


**Figure 1.** Surface analysis of the $CsPbBr_3$ perovskite thin film. (a) AFM topography, (b) 5 keV secondary electron (SE) image, (c) 5 keV CL map ($\lambda$ = 525 nm, 6 nm bandwidth), and (d) schematic of CL measurement geometry and CL spectrum taken from one of the perovskite grains. The scale bar in (a) applies to the three maps.

Notably, however, the CL map shows a reduced intensity at the grain boundaries. Often, reduced emission efficiency at grain boundaries is assigned to nonradiative recombination losses.[3] However, the strong morphological changes should affect the outcoupling of emitted light.[18] This consideration raises the question of whether the change in intensity at the grain boundaries is due to reduced CL radiation quantum efficiency near the grain boundaries or due to an optical effect resulting from variations in outcoupling of the CL emission from the film.

To study the effect of surface topography on the outcoupling of CL emission, we analyze the data for electron energies of 2 and 5 keV. Their corresponding electron−sample interaction volumes differ significantly, with the 5 keV interaction volume extending deeper into the perovskite compared with the 2 keV interaction volume. Figures 2(a,b) show Monte Carlo simulations of primary electron trajectories.[19] The contour lines represent the fraction of the energy density deposited in the film by the cascade of inelastic electron collisions; the yellow and purple regions indicate high- and low-energy secondary electrons, respectively. The 2 keV electrons deposit most of their energy in a ∼30 nm-shallow region beneath the surface, while the 5 keV electrons deposit energy up to ∼150 nm. Similarly, the radial distribution of energy deposition is much wider for 5 keV than for 2 keV irradiation. If the morphology significantly affects CL outcoupling, intensity variations should be more pronounced at 2 keV than at 5 keV, while nonradiative recombination effects remain comparable.

To calculate the CL emission from the corrugated surface topographies, we perform two-dimensional numerical finite-difference time-domain (FDTD) simulations of the electromagnetic near-field and far-field distribution for an array of dipole emitters placed inside the perovskite film. In our analysis, we first consider an internal quantum efficiency of CL emission IQE = 1; afterward we refine our analysis to consider the case IQE ≪ 1. AFM line traces are used as an input for the simulations, and the simulated dipole distribution in the film follows the AFM profile conformally. The far-field emission for each dipole position corresponds to the collected CL intensity of light generated at that position. We calculate the incoherent sum of emission from an array of dipoles (summing contributions of *x*-, *y*-, and *z*-orientated dipoles) inside the interaction volume, weighted by the deposited energy density derived from the Monte Carlo simulations (for details, see the Experimental Section). We then calculate the total angle-integrated far-field radiation intensity to reflect the CL intensity that is collected over the upper hemisphere. Note that we do not consider diffusion of the charge carriers before emission in our simulations; that is, we assume that the emission dipoles are located at the position of excitation with the electron beam.

Figure 2(c) displays the experimental AFM and the normalized CL intensity at the $CsPbBr_3$ bandgap ($\lambda$ = 525 nm, 6 nm bandwidth) at a line trace taken across the maps in Figure 1(a,c) for 5 keV irradiation. Similar data for 2 keV are shown in Figure 2(d). The positions of these traces within the two-dimensional CL maps are shown in Figure S2 in the SI. For both line traces, the AFM profile across the film shows valleys in the surface topography at the positions of the grain boundaries. Comparing the AFM topographies with the CL profiles, a clear correlation between the topographic valleys and CL intensity minima is observed.

Figures 2(c,d) also show the line profiles of the CL emission calculated using the FDTD procedure described above. The overall profile of the calculated CL intensity matches well with


https://doi.org/10.1021/acsenergylett.5c04161
ACS Energy Lett. 2026, 11, 3274−3281

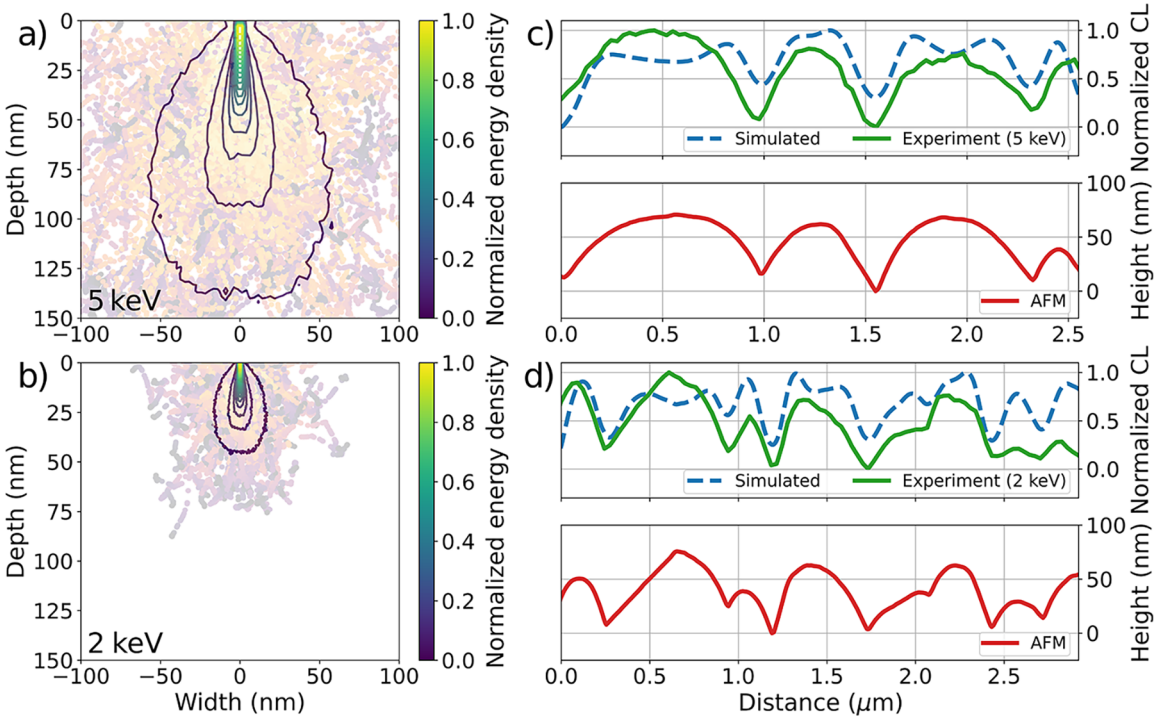


**Figure 2.** (a, b) Monte Carlo simulations of electron cascades in a $CsPbBr_3$ perovskite thin film at (a) 5 keV and (b) 2 keV electron energy.[19] Dots indicate inelastic collisions, and yellow and purple dots indicate high- and low-energy electrons, respectively. The fraction of the energy density deposited in inelastic collisions is indicated by the contour lines. (c, d) Experimental AFM (red) and normalized CL (green) line traces ($\lambda$ = 525 nm, 6 nm bandwidth) across the perovskite film on silicon at (c) 5 and (d) 2 keV, shown together with simulated CL line traces (blue dashed lines). The silicon substrate was positioned 171 and 151 nm below the AFM minimum for the 5 and 2 keV case, respectively, as derived from cross-sectional SEM measurements in Figure S3 in the SI. The experimental CL line trace is plotted with an offset in the *x*-direction to match best with the dips in the grain boundaries in the simulated trace.

the experimental CL line trace. This indicates that the film morphology plays a significant role in determining the CL outcoupling efficiency as no nonradiative recombination was considered in our simulations. The simulations show that the curved surface near grain boundaries enhances internal reflection of light, resulting in increased light trapping within the perovskite film. As a result, when the electron beam is placed near a grain boundary, the outcoupled CL intensity is significantly reduced.

Figure 3(a) shows the CL map (2 keV, $\lambda$ = 525 nm, 6 nm bandwidth) for a $CsPbBr_3$ film with larger grains. The grain sizes range from approximately 1 to 4 $\mu$m, which was achieved by annealing the films at 300 °C for 5 min (see Experimental Section). Here, in addition to the dark bands at the grain boundaries, similar to those seen in Figure 2(c,d), we observe pronounced CL intensity modulations within individual grains. These intragrain patterns show concentric rings with alternating emission intensities for nearly all perovskite grains. Figure 3(b) presents a line trace from the experimental CL map overlaid with a simulation using the AFM profile as input. Just like before, the low CL signal near the grain boundaries is well represented by the simulations, reflecting the reduced outcoupling of CL emission. At the same time, both the experiment and the simulations show a ring of reduced emission near the middle of the grain, with a slight enhancement at its center. This intragrain variation is particularly clear for the large grain represented by the AFM scan between 3 and 4 $\mu$m in Figure 3(b,c).

To study the origin of the intragrain CL modulation in more detail, Figure 3(c) presents a crosscut through perovskite grains using the surface profile from the AFM line trace of Figure 3(b). The color scale indicates the simulated angle-integrated far-field radiation intensity for each dipole position within the perovskite film. The simulations show a clear dependence of the outcoupled CL on the dipole position within the grain. First, the dark regions corresponding to the dark CL bands at the grain boundaries are clearly seen again. Furthermore, outcoupling variations are observed depending on the dipole position inside the grains, both horizontally and vertically. We ascribe the vertical variations to constructive and destructive interference of dipole emission reflecting off the perovskite film surface and the silicon substrate underneath. This reasoning agrees well with the observed fringe period of roughly 100 nm, which is consistent with the thin-film interference period for 525 nm light in a medium with a refractive index of the $CsPbBr_3$ perovskite ($n$ = 2.67).[20]

Figure 3(c) also shows the dimensions of the electron cascades for 2 and 5 keV electrons. The 2 keV excitation volume extends ~30 nm into the film (Figure 2b), and scanning the electron beam across the sample surface thus results in the detection of CL from near-surface regions with intensities that reflect the constructive or destructive interference in the film. This surface-sensitive detection gives rise to the observation of dark and bright rings in the CL map of Figure 3(a). For the 5 keV beam, which penetrates deeper into the film (exceeding 100 nm in depth), the collected CL emission is an average over multiple interference minima and maxima, causing the ring structure to be less pronounced. This phenomenon agrees with the 5 keV CL map in Figure S4 in


https://doi.org/10.1021/acsenergylett.5c04161
ACS Energy Lett. 2026, 11, 3274−3281

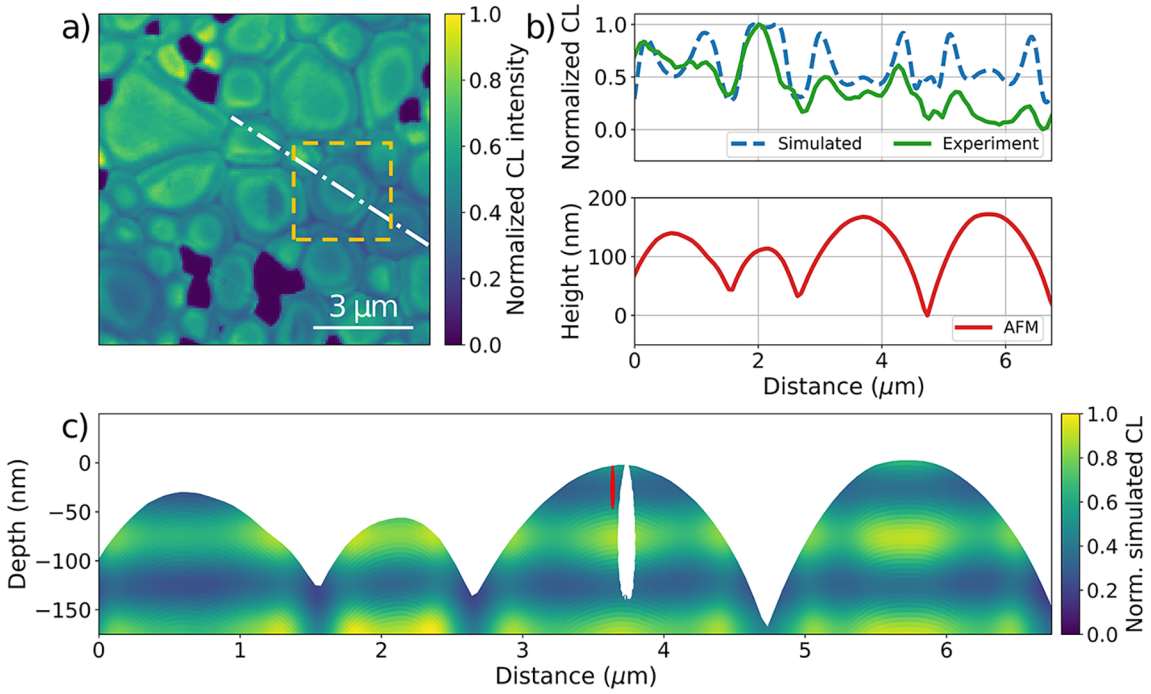


**Figure 3.** (a) Experimental CL map (2 keV, $\lambda$ = 525 nm, 6 nm bandwidth) for a $CsPbBr_3$ film with grain sizes ranging from ~1 to 4 $\mu$m. The white dashed line indicates the line trace for the 2D simulations. The dashed orange square indicates the area that has been simulated in 3D. (b) AFM (red) and experimental CL line traces (green) across the perovskite film, together with the simulated CL line trace (dashed blue line). The experimental line trace is plotted with an offset in the $x$-direction to coincide with the simulated trace at the grain boundaries. (c) Total integrated far-field radiation versus dipole position in the perovskite film placed on a silicon substrate positioned 70 nm below the AFM minimum, based on the crosscut measurements in Figure S3. The 2 and 5 keV interaction volumes of Figure 2(a,b) are displayed in red and white, respectively. Note the different horizontal and vertical length scales in (c).

the SI, in which the rings are less pronounced compared with those in the 2 keV CL map in Figure 3(a).

To further demonstrate that the observed rings originate from interference, we semianalytically calculate the total far-field radiation for a two-dimensional array of dipoles embedded in a planar thin film of perovskite between silicon and air (Figure S8 in the SI). The calculated far-field intensity (Figure S9(a) in the SI) is weighted with the laterally averaged excitation density in the Monte Carlo cascade profiles for 2 and 5 keV electrons (Figure S9(b)), from which we derive the CL emission intensity as a function of dipole depth (Figure S9(c)). We then calculate the weighted far-field CL intensity integrated over depth for different perovskite thicknesses for 2 and 5 keV electrons (Figure S10). This clearly shows the variation of the outcoupled CL intensity with film thickness, confirming the interference model. The lower visibility of the interference rings for 5 keV irradiation that is observed in the experiment (Figure S4 compared to Figure 3(a)) is also confirmed by the calculation in Figure S10.

We note that the CL maps in Figures 2 and 3 show significant grain-to-grain contrast across the film. We assign this to the fact that for smaller grains the effect of reduced outcoupling near grain boundaries will affect the overall CL intensity in a stronger way than for large grains, making the grain appear less bright in some cases. Furthermore, as our model shows, due to interference across the film depth, the CL intensity is strongly dependent on the thickness of each grain, which can also create grain-to-grain contrast.

So far, we have presented an analysis for arrays of dipole emitters in the $x$−$z$ plane, which intersects the line traces in the AFM and CL maps. Next, we study the outcoupling effects in a geometry that extends into the third dimension inside the film. Figure 4(a) displays the AFM topography (top layer) for the grain within the orange dashed square in Figure 3(c). We

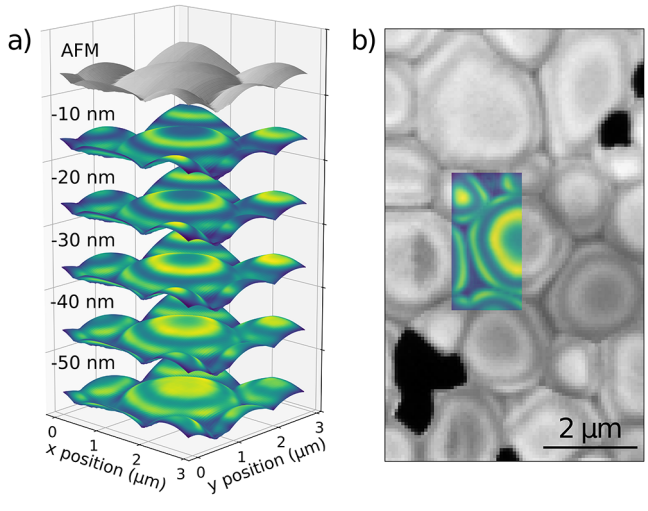


**Figure 4.** (a) Top: AFM map of a large perovskite grain. Colored patterns: simulated integrated far-field CL intensity for an array of dipoles in a sheet conformally following the surface topography positioned at depths of 10, 20, 30, 40, and 50 nm. (b) Experimental CL map (2 keV, $\lambda$ = 525 nm, bandwidth 6 nm, gray scale) for a $CsPbBr_3$ film with grain sizes ranging from ~1 to 4 $\mu$m, with the center grain shown in the AFM map in (a). Overlayed colored region: simulated far-field CL intensity for a sheet of dipoles at 30 nm depth as shown in (a).



https://doi.org/10.1021/acsenergylett.5c04161
ACS Energy Lett. 2026, 11, 3274−3281

simulate the far-field CL intensity for a sheet of dipoles that conformally follows the surface topography at a fixed depth. Data are shown for depths of 10, 20, 30, 40, and 50 nm. At each depth, the concentric rings in the simulated CL emission intensities are clearly visible. Their intensity maxima shift inward as the dipole layer is positioned deeper beneath the surface, as expected for the interference model given the convexly curved surface of the grain (Section S7 in the SI). The simulated CL map for a dipole depth of 30 nm is overlaid on the experimental CL map for 2 keV irradiation in Figure 4(b). It matches very well with the experimental data, in agreement with the fact that 2 keV electrons deposit most of their energy around that depth. This is confirmed by calculations in Figure S11 of the SI, which show the depth of maximum CL emission for 2 keV electrons is 20−30 nm, depending on the perovskite film thickness.

Overall, our analyses show that the trends measured in the CL maps are strongly determined by optical outcoupling variations and interference effects. So far, in the analyses we have assumed unity internal quantum efficiency (IQE = 1), meaning that all energy used in the excitation of dipoles is released in the form of radiation. In Figure S7 we present measurements of the CL lifetime (<50 ps) and PL lifetime (1−2 ns) on the same $CsPbBr_3$ films. The much reduced CL lifetime indicates that the CL measurements are taken in a regime dominated by nonradiative recombination, either due to Auger recombination caused by the high carrier injection rate in the electron cascade or due to rapid carrier diffusion away from the small electron−sample interaction volume.[7] From these data we derive that for the CL emission in the perovskite films studied here IQE ≪ 1.

For the case of IQE ≪ 1 the emission intensity collected from dipoles at a certain position is modulated by the Purcell factor, which is proportional to the local density of optical states (LDOS) (Section S5 in the SI). Indeed, due to the strong index contrast between the perovskite and vacuum and the presence of a high-index substrate, the Purcell factor is modulated across the film.[21−24]

We have simulated the Purcell factor as a function of position in the film, alongside the dipole simulations shown above (Figures S5(b,c,d) and S6(b,c,d) in the SI). We then multiplied the outcoupling maps shown in Figure 2(c,d) with this Purcell factor distribution to represent the limit of IQE ≪ 1 (Figures S5(a) and S6(a) in the SI), which allows a realistic comparison between the experimental values and the computational analysis. We find only a minor effect on the outcoupling line traces, indicating that our analysis is valid for the full range 0 < IQE < 1. While our analysis above is for CL maps, we note that PL maps taken on the same areas as studied above may show (in addition to strong outcoupling effects near the grain boundaries) effects of nonradiative decay at grain boundaries that are obscured in the CL measurements due to the high bulk decay rate under electron irradiation. The low IQE in the present study therefore enables us to independently determine the optical outcoupling effects.

Finally, we address discrepancies observed between the CL measurements and the simulations as well as the impact of certain assumptions made in the simulations. First, we note that the simulated CL traces show a stronger modulation across the surface of a grain than that of the measurements. This discrepancy could arise from the fact that the simulations use a two-dimensional geometry, whereas in reality the three-dimensional surface topography should be taken into account. Small differences in perovskite film thickness between the simulation and experiment could also influence the simulation outcome. Moreover, the Monte Carlo simulations do not capture all details of the electron−matter energy exchange,[25] and carrier diffusion inside and away from the cascade may increase the effective volume from which the CL emission is generated, reducing the CL intensity modulation across the film.

Furthermore, the simulations in Figures 2−4 are carried out using a real-valued refractive index, neglecting optical absorption in the perovskite film. The optical absorption length in the perovskite film is $L_\alpha \approx 267$ nm at the studied wavelength, $\lambda = 525$ nm. Therefore, the effect of absorption on the direct outcoupling of the CL emission will be minimal for the shallow interaction depth at 2 keV (<50 nm) (Figure S9(c) in the SI). For the 5 keV measurements, the interaction volume extends deeper, and therefore, part of the CL emission that is generated deeper in the film will be absorbed, lowering the outcoupled intensity for dipoles generated at larger depth. Absorption in the perovskite does affect the visibility of the interference fringes due to the Fabry−Pérot resonance across the film, as illustrated in Figure S10. Finally, we note that in the limit of high nonradiative recombination the effect of photon recycling can be neglected. We further note that the observation of these interference effects in the 2 keV CL maps indicates that long-range carrier diffusion within the perovskite grains does not dominate the CL signal.

In conclusion, we find that intensity variations in the cathodoluminescence (CL) maps of polycrystalline $CsPbBr_3$ films can be predominantly assigned to changes in outcoupling and interference effects arising from the surface morphology. This finding is in stark contrast to the conventional assumption that variations in local emission intensity stem from changes in the nonradiative recombination and therefore emission efficiency. Our analysis includes the excitation distribution in the electron cascade, the effect of surface geometry on outcoupling of the electron-generated electromagnetic near fields, and the local density of optical states. More broadly, the strong near-field coupling and interference effects observed here are relevant for the analysis of CL and micro-photoluminescence of corrugated films across a wide range of material systems.

## EXPERIMENTAL SECTION

### Perovskite Film Synthesis

The Si substrates were loaded into a PEROevap (CreaPhys) chamber inside a $N_2$-filled glovebox for perovskite evaporation. Two sources, CsBr and $PbBr_2$, were both deposited at 0.25 Å/s to reach a Cs:Pb = 1:1 stoichiometric ratio, which was achieved by independently controlling its own heating unit and quartz crystal microbalance rate sensor. The distance between sources and the substrate holder is around 35 cm. The deposition was done at $2 \times 10^{-6}$ mbar and room temperature for the substrate. After deposition, the samples were annealed on a hot plate for 30 min at 200 °C in air for the films with the smaller grains (0.1−1 μm), and the samples were annealed for 5 min at 300 °C in air for the large grain films (1−4 μm).

### CL and PL Measurements

The CL measurements were performed in a FEI Quanta650 SEM (Thermo Fisher) equipped with a Delmic Sparc CL system consisting of a parabolic mirror to collect the emitted light from the sample within an angular range of 1.42 π sr and a spectrometer with a Andor Newton CCD camera for spectral analysis. For the small-grain samples, an electron beam current of 40 pA was applied, whereas a


https://doi.org/10.1021/acsenergylett.5c04161
ACS Energy Lett. 2026, 11, 3274−3281

current of 85 pA was used for larger grains. The acceleration voltage was varied between 2 and 5 kV to enable different electron−sample interaction volumes. CL maps were recorded with a pixel size of 30 nm at an exposure time of 1 ms for each pixel for the small-grain samples, whereas a pixel size of 70 nm and an exposure time of 10 ms were used for the films with larger grains. For CL lifetime measurements, the electron beam was modulated to create 30 ps electron pulses using an electrostatic beam blanker at a repetition rate of 10 MHz. Time correlated single photon counting (TCSPC) was performed with a PicoQuant hybrid series photomultiplier (PMT) and a PicoQuant PicoHarp 300 correlator with a temporal resolution down to 50 ps. PL decay time measurements were performed using a $\lambda$ = 485 nm pulsed laser (3 MHz, 0.41 $\mu$W) focused with a spot size close to the diffraction limit. Both CL and PL decay traces were recorded by using time-correlated single-photon counting systems.

### AFM Measurements

For the small-grain films, topographical maps were measured on a Bruker Dimension Icon AFM with a ScanAsyst-Air probe with a nominal tip radius of 2 nm (Bruker). For the large-grain films, topographical maps were obtained with a Bruker Dimension FastScan AFM with a ScanAsyst-Air probe with a nominal tip radius of 2 nm (Bruker).

### Numerical Optical Simulations

Finite-difference time-domain (FDTD) simulations were conducted using Lumerical FDTD (Ansys), version 2024 R2.3, with surface topographies from AFM as input. For the 2D simulations, the AFM line traces were interpolated with an interval of 5 nm. The AFM maps for the 3D simulations were interpolated to a grid with half of the original spacing, preserving the original data points. Optical constants for $CsPbBr_3$ ($n$ = 2.67) and Si ($n$ = 4.18) were obtained from Ermoloav et al.[26] and Palik,[27] respectively. All materials in the simulations are assumed to be lossless; therefore, the imaginary part of the refractive index was set to zero. For 2D simulations, dipole sources emitting at $\lambda$ = 525 nm were positioned within the perovskite on a square mesh of 5 nm with 5 nm spacing between the dipoles. To prevent numerical and mesh-related artifacts at the surface, the first dipole line, 5 nm beneath the surface, was excluded in the 5 keV small-grain and 2 keV large-grain simulations. For the second dipole line, a mesh of 3 nm was used to prevent numerical artifacts close to the surface. In the 2 keV small-grain simulations, the first dipole line was included in the analysis by applying a nonuniform mesh of 1 nm around the dipole source. The simulations for 5 keV and the 2 keV large-grain simulations extended to 200 nm beneath the surface, while the 2 keV small-grain simulations extended to 60 nm only. Three polarization directions ($x$, $y$, and $z$) were simulated separately, and the electric and magnetic field vectors were calculated by monitoring several tens of nanometers above the perovskite surface. The simulation time was 1000 fs, and eight perfectly matched boundary layers were used to limit the simulation volume. The near-field distribution was transformed to far-field radiation fields using the built-in near- to far-field transformation in Lumerical. The far fields for each polarization were then incoherently summed to yield the far-field radiation intensity as a function of the angle. Integrating over the full upper hemisphere resulted in total integrated far-field radiation. Once the far-field light intensity distribution was computed for each dipole position, it was convoluted with the 2D energy deposition density of inelastic scattering for 2 and 5 keV electrons, obtained from Monte Carlo electron cascade calculations using CASINO.[19]

The 3D-simulations were performed by using the Snellius supercomputer, hosted by SURF (the collaborative ICT organization for Dutch education and research). In all simulations, dipoles were spaced roughly 29 nm laterally, and each plane was separated 10 nm in height. The transformation to the far field was performed directly in the Lumerical FDTD simulation by placing a field monitor above the surface at a fixed height above the perovskite surface. Again, the fields corresponding to each polarization were incoherently summed and integrated over the full upper hemisphere, yielding the total integrated far-field radiation.

## ■ ASSOCIATED CONTENT

### Supporting Information

The Supporting Information is available free of charge at https://pubs.acs.org/doi/10.1021/acsenergylett.5c04161.

X-ray diffractograms, line traces, 5 keV CL map of the large-grain sample, SEM cross sections, the effect of nonradiative decay rate on simulated line traces, CL and PL lifetime measurements, analytical treatment of dipole emission in an infinite parallel-plate geometry (PDF)

## ■ AUTHOR INFORMATION


### Corresponding Authors

**Robin Schot** − *LMPV-Sustainable Energy Materials Department, AMOLF, Amsterdam 1098 XG, The Netherlands;* orcid.org/0000-0001-9037-0360; Email: r.schot@amolf.nl

**Imme Schuringa** − *LMPV-Sustainable Energy Materials Department, AMOLF, Amsterdam 1098 XG, The Netherlands;* orcid.org/0000-0002-8825-6937; Email: i.schuringa@amolf.nl

### Authors

**Álvaro Rodríguez Echarri** − *LMPV-Sustainable Energy Materials Department, AMOLF, Amsterdam 1098 XG, The Netherlands;* orcid.org/0000-0003-4634-985X

**Lars Sonneveld** − *LMPV-Sustainable Energy Materials Department, AMOLF, Amsterdam 1098 XG, The Netherlands;* orcid.org/0009-0005-2669-9539

**Tom Veeken** − *LMPV-Sustainable Energy Materials Department, AMOLF, Amsterdam 1098 XG, The Netherlands;* orcid.org/0000-0002-6235-7836

**Yang Lu** − *Department of Chemical Engineering and Biotechnology, University of Cambridge, Cambridge CB3 0AS, U.K.;* orcid.org/0000-0002-2793-2065

**Samuel D. Stranks** − *Department of Chemical Engineering and Biotechnology, University of Cambridge, Cambridge CB3 0AS, U.K.;* orcid.org/0000-0002-8303-7292

**Albert Polman** − *LMPV-Sustainable Energy Materials Department, AMOLF, Amsterdam 1098 XG, The Netherlands;* orcid.org/0000-0002-0685-3886

**Bruno Ehrler** − *LMPV-Sustainable Energy Materials Department, AMOLF, Amsterdam 1098 XG, The Netherlands;* orcid.org/0000-0002-5307-3241

**Saskia Fiedler** − *LMPV-Sustainable Energy Materials Department, AMOLF, Amsterdam 1098 XG, The Netherlands;* orcid.org/0000-0002-7753-0814

Complete contact information is available at: https://pubs.acs.org/10.1021/acsenergylett.5c04161


### Author Contributions

S.F., A.P., and B.E. conceived the project. Y.L. and S.D.S. fabricated the perovskite films. S.F. and I.S. carried out and analyzed the CL measurements, R.S. performed numerical simulations with advice from T.V. S.F. and R.S. analyzed the simulation data. L.S. conducted the AFM measurements. A.R.E. performed analytical calculations. S.F. conducted the time-resolved CL measurements. S.F. and R.S. drafted the original manuscript. A.P. and B.E. supervised the project, and all authors reviewed and edited the manuscript.



https://doi.org/10.1021/acsenergylett.5c04161
ACS Energy Lett. 2026, 11, 3274−3281

## Notes

The authors declare the following competing financial interest(s): Albert Polman is cofounder and co-owner of Delmic BV, a company that produces commercial cathodoluminescence systems like the one that was used in this work.

## ■ ACKNOWLEDGMENTS

The authors acknowledge Daphne Dekker for conducting the time-resolved PL measurements. This work is part of the research program of the Dutch Research Counsil (NWO) and SolarLab within SolarNL, a national research, innovation and industrial development program funded by The Netherlands National Growth Fund. It is financed by the European Research Council (ERC) under Grant Agreement No. 101019932 (QEWS), the European Innovation Counsel (EIC) under Grant Agreements No. 101017720 (EBEAM), No. 101151994 (EXPLEIN), and No. 947221 (SHAPE) under the European Union's Horizon 2020 Research and Innovation Program, and the Engineering and Physical Sciences Research Council (EPSRC) for funding (EP/S030638/1, EP/V06164X/1). S.D.S. acknowledges the Royal Society and Tata Group (UF150033, URF\R\221026). This work was supported by the Henry Royce Institute for advanced materials through the Equipment Access Scheme enabling access to Ambient Cluster Tool facilities at Cambridge [the EPSRC (EP/R00661X/1) and Cambridge Royce facilities grant EP/P024947/1]. This work used the Dutch national e-infrastructure with the support of the SURF Cooperative using grant no. EINF-11575.

## ■ REFERENCES

(1) Green, M. A.; Dunlop, E. D.; Yoshita, M.; Kopidakis, N.; Bothe, K.; Siefer, G.; Hinken, D.; Rauer, M.; Hohl-Ebinger, J.; Hao, X. Solar Cell Efficiency Tables (Version 64). *Progress in Photovoltaics: Research and Applications* **2024**, *32* (7), 425−441.

(2) Sherkar, T. S.; Momblona, C.; Gil-Escrig, L.; Ávila, J.; Sessolo, M.; Bolink, H. J.; Koster, L. J. A. Recombination in Perovskite Solar Cells: Significance of Grain Boundaries, Interface Traps, and Defect Ions. *ACS Energy Lett.* **2017**, *2* (5), 1214−1222.

(3) Quirk, J.; Rothmann, M.; Li, W.; Abou-Ras, D.; McKenna, K. P. Grain Boundaries in Polycrystalline Materials for Energy Applications: First Principles Modeling and Electron Microscopy. *Appl. Phys. Rev.* **2024**, *11* (1), DOI: 10.1063/5.0175150.

(4) Caprioglio, P.; Caicedo-Dávila, S.; Yang, T. C. J.; Wolff, C. M.; Peña-Camargo, F.; Fiala, P.; Rech, B.; Ballif, C.; Abou-Ras, D.; Stolterfoht, M.; Albrecht, S.; Jeangros, Q.; Neher, D. Nano-Emitting Heterostructures Violate Optical Reciprocity and Enable Efficient Photoluminescence in Halide-Segregated Methylammonium-Free Wide Bandgap Perovskites. *ACS Energy Lett.* **2021**, *6* (2), 419−428.

(5) Jagadamma, L. K.; Edwards, P. R.; Martin, R. W.; Ruseckas, A.; Samuel, I. D. W. Nanoscale Heterogeneity in CsPbBr3and CsPbBr3:KI Perovskite Films Revealed by Cathodoluminescence Hyperspectral Imaging. *ACS Appl. Energy Mater.* **2021**, *4* (3), 2707−2715.

(6) Guthrey, H.; Moseley, J. A Review and Perspective on Cathodoluminescence Analysis of Halide Perovskites. *Adv. Energy Mater.* **2020**, *10* (26), 1−33.

(7) Nekita, S.; Yanagimoto, S.; Sannomiya, T.; Akiba, K.; Takiguchi, M.; Sumikura, H.; Takagi, I.; Nakamura, K. G.; Yip, S. P.; Meng, Y.; Ho, J. C.; Okuyama, T.; Murayama, M.; Saito, H. Diffusion-Dominated Luminescence Dynamics of CsPbBr3 Studied Using Cathodoluminescence and Microphotoluminescence Spectroscopy. *Nano Lett.* **2024**, *24* (13), 3971−3977.

(8) Li, J.; Huang, J.; Ma, F.; Sun, H.; Cong, J.; Privat, K.; Webster, R. F.; Cheong, S.; Yao, Y.; Chin, R. L.; Yuan, X.; He, M.; Sun, K.; Li, H.; Mai, Y.; Hameiri, Z.; Ekins-Daukes, N. J.; Tilley, R. D.; Unold, T.; Green, M. A.; Hao, X. Unveiling Microscopic Carrier Loss Mechanisms in 12% Efficient Cu2ZnSnSe4 Solar Cells. *Nat. Energy* **2022**, *7* (8), 754−764.

(9) Abou-Ras, D.; Nikolaeva, A.; Krause, M.; Korte, L.; Stange, H.; Mainz, R.; Simsek Sanli, E.; van Aken, P. A.; Sugaya, T.; Nishinaga, J. Optoelectronic Inactivity of Dislocations in Cu(In,Ga)Se2 Thin Films. *Physica Status Solidi - Rapid Research Letters* **2021**, *15* (7), 1−5.

(10) Ferrer Orri, J. Exploring the Structural and Optical Response of Halide Perovskites Using High Energy Electrons "Seeing with Electrons". Doctoral Thesis, University of Cambridge, 2023.

(11) Klein-Kedem, N.; Cahen, D.; Hodes, G. Effects of Light and Electron Beam Irradiation on Halide Perovskites and Their Solar Cells. *Acc. Chem. Res.* **2016**, *49* (2), 347−354.

(12) Kulbak, M.; Gupta, S.; Kedem, N.; Levine, I.; Bendikov, T.; Hodes, G.; Cahen, D. Cesium Enhances Long-Term Stability of Lead Bromide Perovskite-Based Solar Cells. *J. Phys. Chem. Lett.* **2016**, *7* (1), 167−172.

(13) Rico-Yuson, C. A.; Danwittayakul, S.; Kumar, S.; Hornyak, G. L.; Bora, T. Sequential Dip-Coating of CsPbBr3 Perovskite Films in Ambient Conditions and Their Photovoltaic Performance. *J. Mater. Sci.* **2022**, *57* (22), 10285−10298.

(14) Qaid, S. M. H.; Ghaithan, H. M.; Al-Asbahi, B. A.; Aldwayyan, A. S. Ultra-Stable Polycrystalline CsPbBr3 Perovskite−Polymer Composite Thin Disk for Light-Emitting Applications. *Nanomaterials* **2020**, *10* (12), 1−14.

(15) Dursun, I.; De Bastiani, M.; Turedi, B.; Alamer, B.; Shkurenko, A.; Yin, J.; El-Zohry, A. M.; Gereige, I.; AlSaggaf, A.; Mohammed, O. F.; Eddaoudi, M.; Bakr, O. M. CsPb2Br5 Single Crystals: Synthesis and Characterization. *ChemSusChem* **2017**, *10* (19), 3746−3749.

(16) Ezzeldien, M.; Al-Qaisi, S.; Alrowaili, Z. A.; Alzaid, M.; Maskar, E.; Es-Smairi, A.; Vu, T. V.; Rai, D. P. Electronic and Optical Properties of Bulk and Surface of CsPbBr3 Inorganic Halide Perovskite a First Principles DFT 1/2 Approach. *Sci. Rep.* **2021**, *11* (1), 1−12.

(17) He, X.; Qiu, Y.; Yang, S. Fully-Inorganic Trihalide Perovskite Nanocrystals: A New Research Frontier of Optoelectronic Materials. *Adv. Mater.* **2017**, *29* (32) DOI: 10.1002/adma.201700775.

(18) Qi, H.; Wang, H.; Chen, Y.; Zhang, L.; Wu, J.; Li, T.; Li, W.; Wang, K.; Wang, H.; Tong, Y. Synchronous Optimization of Light Outcoupling and Carrier Recombination for Efficient and Spectral Stable Blue Perovskite Light-Emitting Diodes. *Adv. Funct. Mater.* **2024**, *34* (28), 1−8.

(19) Drouin, D.; Couture, A. R.; Joly, D.; Tastet, X.; Aimez, V.; Gauvin, R. CASINO V2.42 - A fast and easy-to-use modeling tool for scanning electron microscopy and microanalysis users. *Scanning* **2007**, *29* (3), 92−101.

(20) Hecht, E. *Optics*, 5th ed. Pearson Education, 2017.

(21) Kalkman, J.; Gersen, H.; Kuipers, L.; Polman, A. Excitation of Surface Plasmons at a Si O2 Ag Interface by Silicon Quantum Dots: Experiment and Theory. *Phys. Rev. B Condens. Matter Mater. Phys.* **2006**, *73* (7), 1−8.

(22) Walters, R. J.; Kalkman, J.; Polman, A.; Atwater, H. A.; De Dood, M. J. A. Photoluminescence Quantum Efficiency of Dense Silicon Nanocrystal Ensembles in Si O2. *Phys. Rev. B Condens. Matter Mater. Phys.* **2006**, *73* (13), 2−5.

(23) Snoeks, E.; Lagendijk, A.; Polman, A. Measuring and Modifying the Spontaneous Emission Rate of Erbium near an Interface. *Phys. Rev. Lett.* **1995**, *74* (13), 2459−2462.

(24) Drexhage, K. H. Influence of a Dielectric Interface on Fluorescence Decay Time. *J. Lumin.* **1970**, *1−2* (C), 693−701.

(25) Arat, K. T.; Klimpel, T.; Hagen, C. W. Model Improvements to Simulate Charging in Scanning Electron Microscope. *Journal of Micro/Nanolithography, MEMS, and MOEMS* **2019**, *18* (04), 1.

(26) Ermolaev, G.; Pushkarev, A. P.; Zhizhchenko, A.; Kuchmizhak, A. A.; Iorsh, I.; Kruglov, I.; Mazitov, A.; Ishteev, A.; Konstantinova, K.; Saranin, D.; Slavich, A.; Stosic, D.; Zhukova, E. S.; Tselikov, G.; Di Carlo, A.; Arsenin, A.; Novoselov, K. S.; Makarov, S. V.; Volkov, V. S. Giant and Tunable Excitonic Optical Anisotropy in Single-Crystal Halide Perovskites. *Nano Lett.* **2023**, *23* (7), 2570−2577.

(27) Palik, E. *Handbook of Optical Constants of Solids*; Elsevier Science Publishing, 1991.



https://doi.org/10.1021/acsenergylett.5c04161
*ACS Energy Lett.* 2026, 11, 3274−3281